

Room-temperature spin-orbit torque switching in a manganite-based heterostructure

Liang Liu^{1,*}, Guowei Zhou^{2,*}, Xinyu Shu¹, Changjian Li^{1,3}, Weinan Lin^{1,4}, Lizhu Ren⁵, Chenghang Zhou,¹ Teyang Zhao,¹ Rui Guo,¹ Qidong Xie,¹ Han Wang,¹ Jing Zhou,¹ Ping Yang,^{1,6} Stephen J. Pennycook¹, Xiaohong Xu,^{2,†} and Jingsheng Chen^{1,7,8,9,‡}

¹*Department of Materials Science and Engineering, National University of Singapore, Singapore 117575, Singapore*

²*Key Laboratory of Magnetic Molecules and Magnetic Information Materials of Ministry of Education, School of Chemistry and Materials Science, Shanxi Normal University, Taiyuan 041004, China*

³*Department of Materials Science and Engineering, Southern University of Science and Technology, Shenzhen 518055, China*

⁴*Department of Physics, Xiamen University, Xiamen 361005, China*

⁵*Department of Electrical and Computer Engineering, National University of Singapore, Singapore 117575, Singapore*

⁶*Singapore Synchrotron Light Source (SSLS), National University of Singapore, 5 Research Link, Singapore 117603, Singapore*

⁷*Suzhou Research Institute, National University of Singapore, Suzhou 215123, China*

⁸*Chongqing Research Institute, National University of Singapore, Chongqing 401120, China*

⁹*Institute of Material Research and Engineering, Agency for Science, Technology and Research (A*STAR), Singapore 138634, Singapore*



(Received 4 November 2021; revised 18 January 2022; accepted 29 March 2022; published 14 April 2022)

The oxide ferromagnet $\text{La}_{0.67}\text{Sr}_{0.33}\text{MnO}_3$ (LSMO) possesses low saturation magnetization (M_s), a low magnetic damping constant (α), and high carrier spin polarization, which promise superior functionalities in spintronics devices. For applications, these devices are to be integrated into electronic circuits, which require the control of the magnetization of LSMO by electrical means. However, a reliable electrical switching method remains largely unexplored. Here, we study the current-induced spin-orbit torque (SOT) in an all-oxide $\text{SrIrO}_3/\text{LSMO}$ bilayer. We found the magnetization of a 15 nm LSMO can be switched by electrical current, as confirmed from both the electrical transport measurement and the magnetic optical measurement. By taking advantage of the strain-mediated magnetic anisotropy, the magnetic easy axis of LSMO was controlled to be either perpendicular or parallel to the charge current direction such that a type- y or a type- x SOT switching was achieved, respectively. The dampinglike SOT efficiency is characterized to be 0.15 at room temperature according to the harmonic Hall voltage analysis. We also studied the temperature dependences of the SOT effective field and current-induced switching. Our demonstration of the electrical switching of LSMO magnetization at room temperature may stimulate SOT studies in a wide variety of all-oxide systems.

DOI: [10.1103/PhysRevB.105.144419](https://doi.org/10.1103/PhysRevB.105.144419)

I. INTRODUCTION

Accompanied with the intense study of the spin Hall and/or the Rashba-Edelstein effects in heavy metal/ferromagnet (HM/FM) [1,2] and topological insulator/FM [3] heterostructures, growing interest has also been drawn on corresponding spin-orbit phenomena in oxide-based heterostructures. In general, the HM layer can be replaced by an oxide material with strong spin-orbit coupling for spin-orbit torque (SOT) studies. For example, researchers have investigated the inverse spin Hall effect in indium tin oxide/Py [4] and IrO_2/Py [5], the inverse Edelstein effect in $\text{SrTiO}_3/\text{LaAlO}_3/\text{Py}$ [6], and the spin-torque FM resonance in SrIrO_3/Py [7,8], $\text{Sr}_2\text{IrO}_4/\text{Py}$ [8], SrRuO_3/Co [9], and SrRuO_3/Py [10,11]. According to these studies, SrIrO_3 , SrRuO_3 , and $\text{LaAlO}_3/\text{SrTiO}_3$ have been identified as three efficient spin sources. On the other side, oxide materials have been extensively used as the magnetic free layer. For instance, previous studies have demonstrated the

current-induced magnetization switching in Pt/yttrium iron garnet (YIG) [12], Pt/TmIG [13], Pt/NiO [14], and Pt/ $\alpha\text{-Fe}_2\text{O}_3$ [15] and the spin transport in $\text{Pt}/\text{La}_{0.67}\text{Sr}_{0.33}\text{MnO}_3$ (LSMO) [16] and $\text{Pt}/\text{Cr}_2\text{O}_3$ [17]. Compared with metallic magnetic layers, oxide magnetic layers possess superior spintronics properties such as the ultra-low magnetic damping constant (YIG [18], LSMO [19]) and the ultra-long spin-transmission length (YIG [20], NiO [21], $\alpha\text{-Fe}_2\text{O}_3$ [22]). Considering the multitude of oxides that can be selected for spin-source layers and magnetic free layers, all-oxide SOT heterostructures have emerged as hotspots [23–29]. They can offer ideal platforms to explore the intrinsic charge-to-spin interconversion due to the minimized interfacial spin scattering [26]. The capability of the nearly single-crystal growth in all-oxide heterostructures also provides exceptional opportunities to engineer strain-mediated magnetic anisotropy and to study the crystal symmetry-dependent SOT efficiency [24]. For these purposes, efficient charge-spin interconversion effects were reported in all-oxide heterostructures, including $\text{SrRuO}_3/\text{LSMO}$ [23], $\text{SrIrO}_3/\text{SrRuO}_3$ [24], $\text{LaAlO}_3/\text{SrTiO}_3/\text{LSMO}$ [25,27], $\text{SrIrO}_3/\text{LSMO}$ [26,29], and $\text{SrRuO}_3/\text{YIG}$ [28]. Recently, the current-induced SOT switching was achieved in $\text{SrIrO}_3/\text{SrRuO}_3$ at 70 K [24]. However,

*L.L. and G.Z. contributed equally to this paper.

†xuxh@sxnu.edu.cn

‡msecj@nus.edu.sg

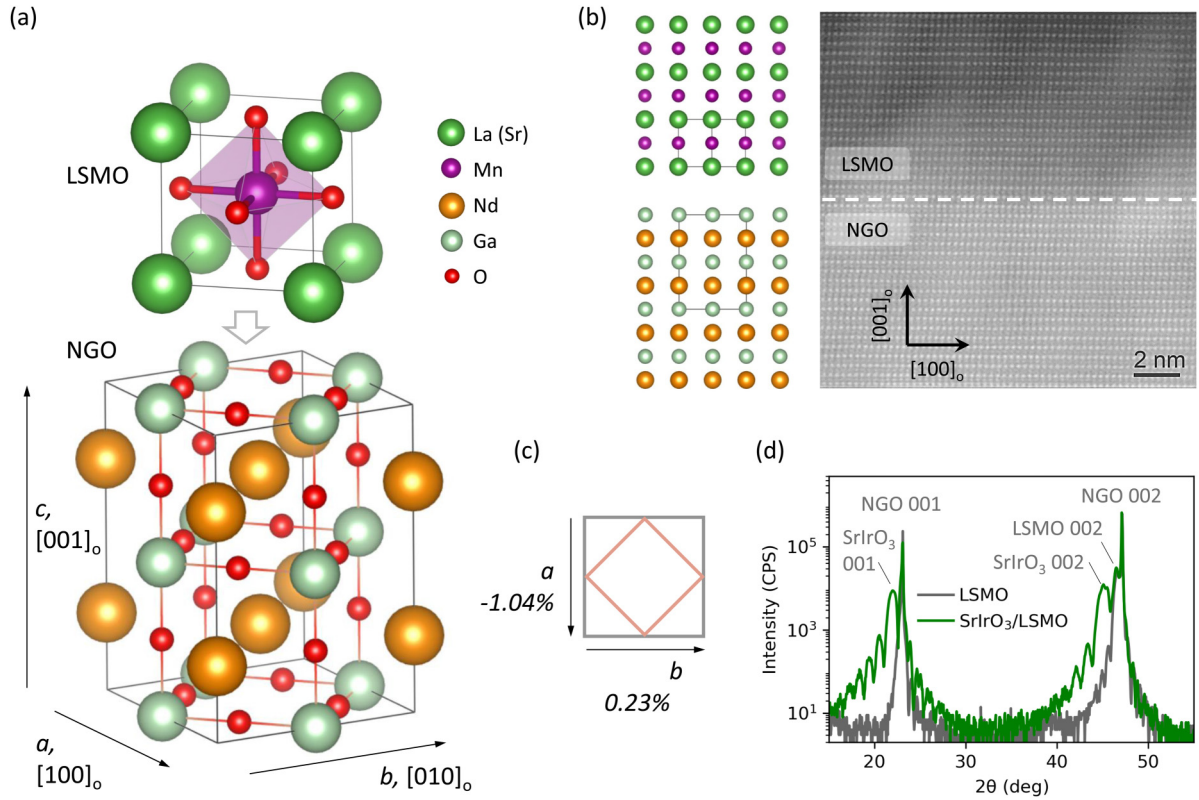


FIG. 1. Structural properties. (a) Schematic illustration of the growth type for LSMO on NGO (001) substrate. (b) Cross-sectional high-angle annular dark-field scanning transmission electron microscopy (STEM) image near the LSMO/NGO interface. The corresponding schematic drawings of LSMO and NGO are shown on the left, where the cubic unit and orthorhombic unit are indicated. The slant in the STEM is due to sample position drift during image acquisition. (c) Calculated lattice mismatches along the a and b axes of NGO. The gray and orange frames are denoted for NGO and LSMO, respectively. (d) θ - 2θ x-ray diffraction scan of the SrIrO₃ (8 nm)/LSMO (15 nm) bilayer and the LSMO (15 nm) single layer on NGO (001) substrate.

the low Curie temperature (T_C) of SrRuO₃ limits its practical applications. In addition to SrRuO₃, LSMO is another widely used oxide FM but with a T_C higher than room temperature. In this paper, we demonstrate the room-temperature SOT switching in a SrIrO₃/LSMO bilayer.

II. METHODS

A. Material fabrication

The high-quality SrIrO₃ (8 nm)/LSMO (15 nm) bilayer was grown on the NdGaO₃ (001) substrate by a pulsed laser deposition system. Before the deposition, the NGO substrates were annealed at 975 °C for 3 h. During the deposition, *in situ* reflection high-energy electron diffraction was used to monitor the quality of SrIrO₃/LSMO bilayers. These bilayers were grown using a 248 nm KrF excimer laser with the energy density as 1.5 J/cm² and the pulse frequency as 2 Hz. The growth temperature and oxygen pressures were 950 °C and 200 mTorr for the LSMO layer and 750 °C and 100 mTorr for the SrIrO₃ layer, respectively. To avoid oxygen vacancies, these bilayers were cooled to room temperature at 15 °C/min in a 100 Torr oxygen pressure. Then the SiO₂ (2 nm) film was covered on the SrIrO₃/LSMO bilayer using an *in situ* magnetron sputtering system. For the electrical transport measurement, the bilayer was patterned into a 20 μm Hall bar by laser writing. Ar ion milling was used for etching.

III. EXPERIMENTAL RESULTS

A. Control of magnetic anisotropy in SrIrO₃/LSMO heterostructures

As shown in Fig. 1(a), NGO has an orthorhombic crystal structure with the lattice parameters of $a = 5.43$ Å, $b = 5.50$ Å, and $c = 7.71$ Å. LSMO has a rhombohedral structure which is generally described as a pseudocubic structure with a lattice constant of 3.873 Å. When deposited on NGO (001) substrate, the LSMO cube would rotate 45° in plane to match the structure of NGO [Fig. 1(a)]. Therefore, the lattice directions $[110]_{pc}$, $[-110]_{pc}$, and $[001]_{pc}$ for LSMO are aligned with $[100]_o$, $[010]_o$, and $[001]_o$ for NGO, respectively, where the subscripts pc and o denote the pseudocubic structure and orthorhombic structure, respectively. In a bulk form, $d_{(110)} = d_{(-110)} = 5.477$ Å for LSMO. Figure 1(b) shows the cross-sectional schematic drawing (left) and high-angle annular dark-field scanning transmission electron microscopy (STEM) image (right) of the LSMO/NGO interface. The STEM image shows a well-crystallized growth of the thin film with a sharp LSMO/NGO interface. Based on the lattice parameters, we can define the in-plane lattice mismatch between LSMO and NGO as $m_x = (x_{NGO} - x_{LSMO})/x_{LSMO}$, where $x(=a, b)$ is the in-plane lattice constant. As shown in Fig. 1(c), the calculated lattice mismatches are -1.04% (compressive) and 0.23% (tensile) along the $[100]_o$ direction

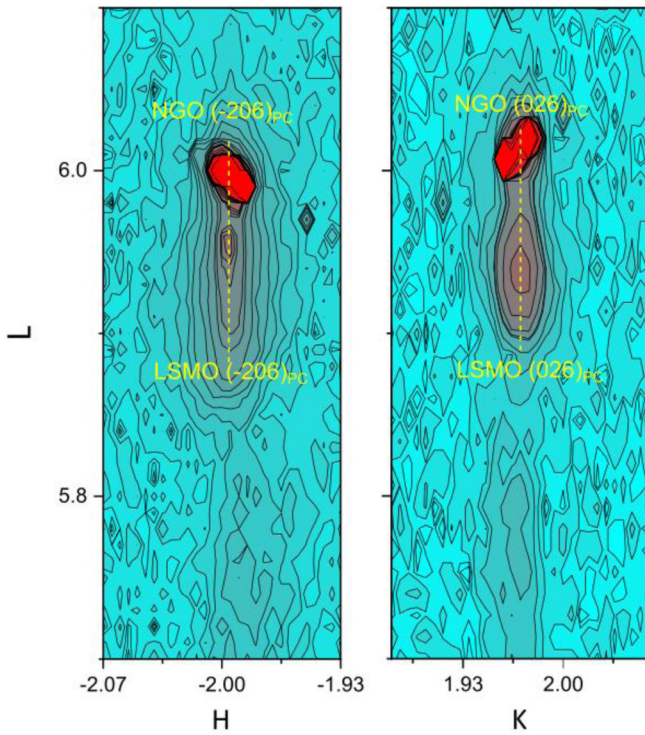


FIG. 2. X-ray reciprocal space mapping of (-206) and (026) peaks for the SrIrO_3 (8 nm)/LSMO (15 nm) film.

(a axis) and the $[010]_o$ direction (b axis), respectively [30]. To experimentally verify this, we carried out x-ray reciprocal space mapping (RSM) on the sample. Figure 2 shows the RSM of (-206) and (026) diffraction peaks for the SrIrO_3 (8 nm)/LSMO (15 nm) sample. As indicated by the yellow dashed line, the LSMO film nearly has the same lattice constant as the NGO substrate, which means the LSMO layer is almost fully strained to the NGO substrate. According to the data, the lattice constants $d_{(110)}$ and $d_{(-110)}$ for the LSMO thin film were calculated to be 5.445 and 5.496 Å, respectively. By comparing these two values with the lattice constant in bulk LSMO (5.477 Å), we confirmed the compressive (tensile) strain from the NGO substrate to the LSMO film in the $[100]_o$ ($[010]_o$) direction. Figure 1(d) shows the θ - 2θ x-ray diffraction patterns for the SrIrO_3 (8 nm)/LSMO (15 nm) and an LSMO (15 nm) single layer. Both of them exhibited LSMO (002) peaks with Laue oscillations, which confirmed the high quality of the LSMO layers. Compared with the LSMO single layer, the SrIrO_3 /LSMO bilayer has extra SrIrO_3 (001) and SrIrO_3 (002) peaks, which indicated the desired epitaxial growth of SrIrO_3 on LSMO.

The unequal in-plane strains from NGO to LSMO were reported to produce an in-plane uniaxial magnetic anisotropy with an easy axis (EA) along the $[010]_o$ direction [31,32]. We measured the magnetization (M) as a function of the in-plane magnetic field (H) along the $[100]_o$ and $[010]_o$ directions, as shown in Fig. 3(a). We observed a squared M - H loop along the

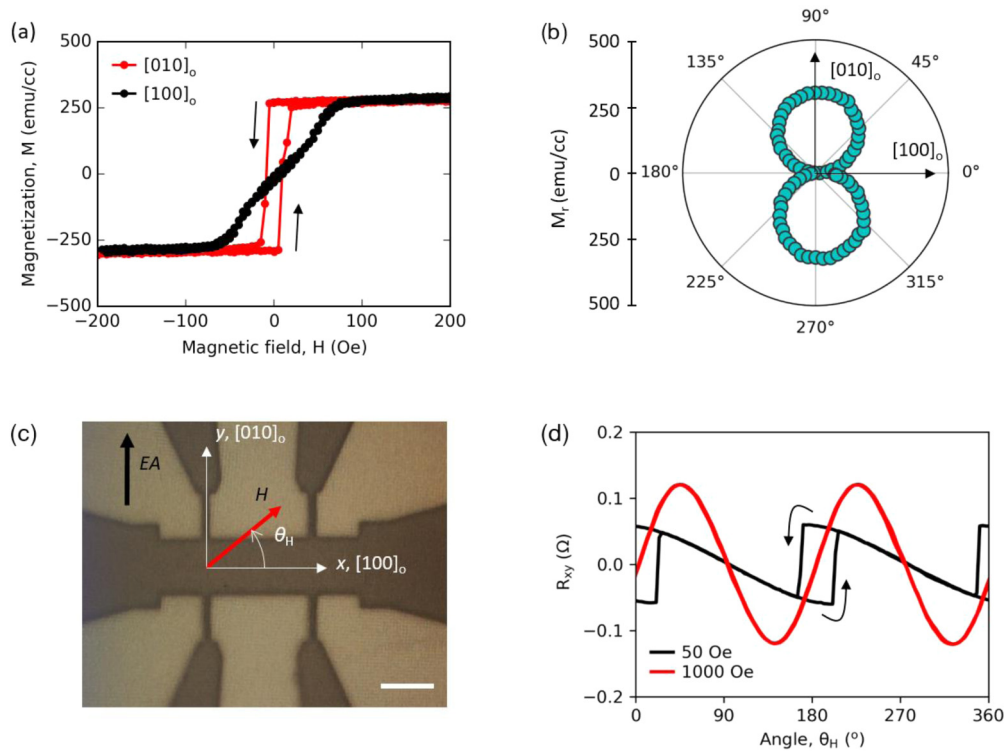


FIG. 3. Magnetic properties of the SrIrO_3 /LSMO bilayer. (a) In-plane magnetic hysteresis loops along the $[010]_o$ direction (red) and the $[100]_o$ direction (dark). (b) Angle dependence of remanent magnetization (M_r). For each data point of M_r , we first applied a magnetic field of 1000 Oe to the saturation magnetization. Then the field was swept down to zero, and the remanent magnetization was measured. (c) Optical image of the Hall bar. The easy axis (EA) was aligned with the y ($[010]_o$) direction. The scale bar at the bottom of the image is $20 \mu\text{m}$. (d) Angle dependence of the Hall resistance under the magnetic fields of 50 Oe (black) and 1000 Oe (red).

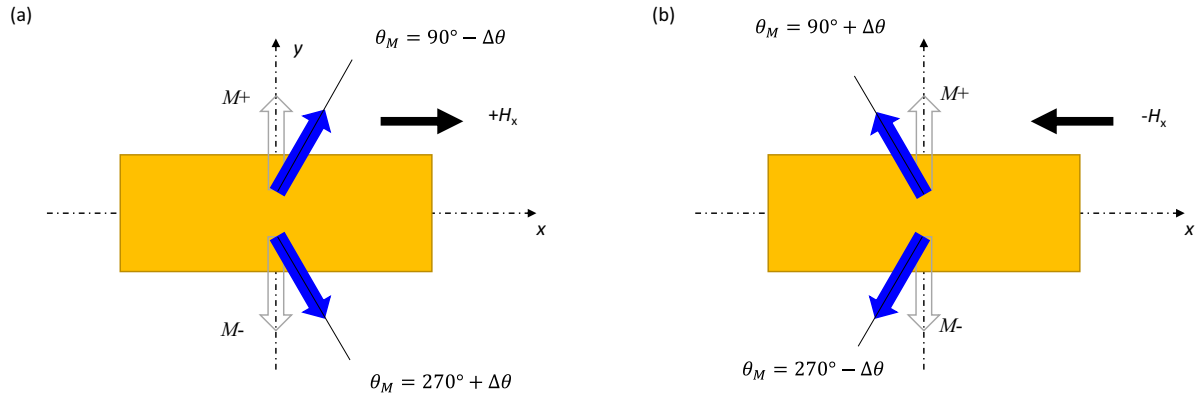


FIG. 4. Principle for the differential planar Hall effect (PHE) measurement: (a) When $+H_x$ is applied, the magnetization $M+$ at 90° will rotate clockwise, which gives a reduction of the azimuth angle of the magnetization ($\theta_M = 90^\circ - \Delta\theta$) and an increased $R_{xy}^{+H_x}$ according to the PHE characteristic in Fig. 3(d), whereas if the magnetization is at 270° ($M-$), the application of $+H_x$ will lead to the decrease of θ_M ($270^\circ + \Delta\theta$), and a decreased $R_{xy}^{+H_x}$ will be measured. (b) On the contrary, when $-H_x$ is applied, a decreased (increased) $R_{xy}^{-H_x}$ will be measured for $M+$ ($M-$).

$[010]_o$ direction and an approximately linear M - H dependence along the $[100]_o$ direction, which are typical features of an in-plane uniaxial magnetic anisotropy. The saturation magnetization M_s is ~ 270 emu/cc. In Fig. 3(b), we measured the remanent magnetization (M_r) as a function of the azimuthal angle (θ_H) between the magnetic field and the $[100]_o$ direction. A twofold symmetry was observed in the $M_r - \theta_H$ plot with the M_r maximizing along the $[010]_o$ axes, which further confirms that the EA is in the $[010]_o$ direction. To study the electrical transport property, the SrIrO₃/LSMO bilayer was fabricated into $20 \mu\text{m}$ Hall bars [Fig. 3(c)].

In a SOT bilayer, the current-induced antidamping torque [$\tau_{\text{AD}} = \mathbf{M} \times (\boldsymbol{\sigma} \times \mathbf{M})$] is aligned with the spin polarization $\boldsymbol{\sigma}$ (y direction), which is orthogonal to the charge current direction (\mathbf{x}). If the EA of M is in the y direction, τ_{AD} can deterministically switch M without the need of an external magnetic field [1] (denoted as type- y switching), whereas if the EA is in the x (z) direction, an external magnetic field along z (x) direction is required to break the symmetry and realize the deterministic magnetization switching (denoted as type- x and type- z switching, respectively) [33]. In HM/FM bilayer with in-plane magnetization, the shape anisotropy is usually dominating (especially for polycrystalline samples), which gives an EA along the current channel unless specific structure confinements (elliptical pillars [1] or isolation bars [34]) are applied. As a comparison, all-oxide heterostructures offer the opportunity to easily tune the EA direction with respect to the current channel direction. Since the EA of the LSMO was in the $[010]_o$ direction, we were able to prepare two types of SrIrO₃/LSMO Hall bars with the EA of the magnetization perpendicular (parallel) to the current channel, which can be used for type- y (type- x) SOT switching. Figure 3(c) shows the Hall bar for type- y SOT switching. We firstly measured the Hall resistance (R_{xy}) as a function of the in-plane angle θ_H under the in-plane magnetic fields of 50 and 1000 Oe [Fig. 3(d)]. Under a magnetic field of 1000 Oe, the magnetization is fully saturated in all directions so that we observed a coherent magnetization rotation process, whereas the 50 Oe magnetic field is not enough to saturate the magnetization along the hard axis [see Fig. 3(a)]. Therefore,

when the magnetization clockwise (anticlockwise) rotates by the hard axis (0° , 180° , or 360°), the Hall resistance will jump up (down) due to the sudden change of the magnetization angle. This is evidenced by the black hysteresis loops in Fig. 3(d).

B. Current-induced magnetization switching

Next, we present the current-induced type- y SOT switching in SrIrO₃/LSMO by performing the electrical transport and the magnetic optical measurements. For the electrical approach, we probe the in-plane magnetization states by using a differential planar Hall effect (PHE) method [35,36]. The principle is that, when we apply a small magnetic field H_x along the x direction [Fig. 4(a)], the magnetization $M+$ ($M-$) initialized at 90° (270°) will rotate clockwise (anticlockwise), which gives an increase (decrease) of R_{xy} according to the PHE characteristic [see Fig. 3(d)]. Similarly, when a negative field $-H_x$ is applied [Fig. 4(b)], the magnetization $M+$ ($M-$) will rotate anticlockwise (clockwise), which gives a reduction (increase) of R_{xy} . In Fig. 5(a), we illustrated the measurement setup for the type- y switching in SrIrO₃/LSMO. In Fig. 5(b), we measured R_{xy} as a function of H_x , and we found two $R_{xy} - H_x$ relations with positive and negative slopes for $M+$ and $M-$, respectively. We can define the change of the Hall resistance as $\Delta R_{xy} = R_{xy}^{+H_x} - R_{xy}^{-H_x}$ for a specific H_x . When a positive (negative) value of ΔR_{xy} is measured, the magnetization is identified to be $M+$ ($M-$). In Fig. 5(c), we used a H_x of 30 Oe and measured ΔR_{xy} by sweeping H_y , which is along the EA direction. The observed $\Delta R_{xy} - H_y$ loop indicates a magnetic-field-induced magnetization switching with a switching field (H_{sw}) of 15 Oe, which is consistent with the squared M - H loop in Fig. 3(a). Then we applied a current pulse (I_{pulse}) to replace the role of H_y and drive the magnetization switching. The pulse duration is 30 μs . As shown in Fig. 5(d), when we swept I_{pulse} in the range from -8 to 8 mA, the magnetization could be deterministically switched. Here, I_{pulse} is the total (terminal) current for the bilayer. The corresponding current density of switching (J_{sw}) in SrIrO₃ is 2.9×10^6 A/cm². For further study, we performed the magnetic

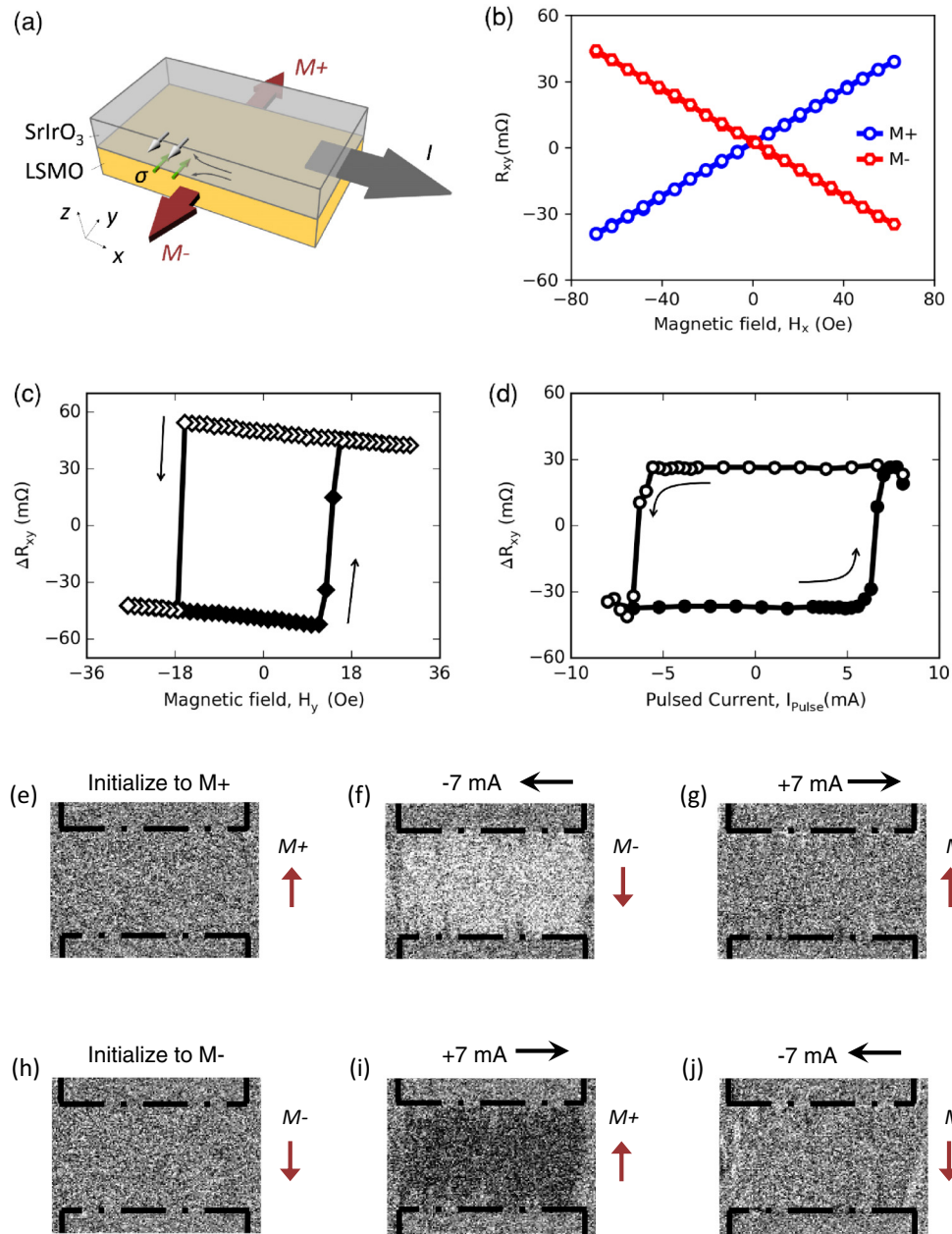


FIG. 5. Current-induced type-y spin-orbit torque (SOT) switching in SrIrO₃/LSMO bilayer. (a) Schematic illustrations of the SOT switching. σ is the spin polarization. (b) Hall resistance as a function of H_x . (c) Magnetic-field-induced switching of the magnetization. (d) Current-induced switching of the magnetization. (e)–(j) Magnetic optical Kerr effect (MOKE) imaging of the LSMO magnetization during SOT switching. The black dot-dashed line outlines the SrIrO₃/LSMO bar device. For processes (e)–(g), the magnetization was first initialized to $M+$ (e). Then the background signal in the whole image was subtracted to enhance the contrast, and the gray color in the bar area represents an $M+$ state. After that, we applied (f) -7 mA and (g) $+7$ mA pulsed current, and the color of the bar turned white (representing $M-$) and gray (representing $M+$), respectively. For processes (h)–(j), the magnetization was first initialized to $M-$ (h). Then we applied (i) $+7$ mA and (j) -7 mA pulsed current, and the color of the bar turned black (representing $M+$) and gray (representing $M-$), respectively. The channel width is $20 \mu\text{m}$.

optical measurement to directly check the magnetic domains during switching. In this approach, the magnetization was captured by magnetic optical Kerr effect (MOKE) imaging. For the processes as shown in Figs. 5(e)–5(g), we first applied a magnetic field $+H_x$ of 100 Oe to saturate the magnetization state to $M+$ [Fig. 5(e)]. Secondly, we applied a I_{pulse} of -7 mA and the bar area changed to white color, representing an

$M-$ state [Fig. 5(f)]. In the third step [Fig. 5(g)], a I_{pulse} of $+7$ mA can switch the magnetization back to $M+$ (gray color). For Figs. 5(h)–5(j), we first initialized the magnetization to $M-$ [Fig. 5(h)]. Then by successively applying $+7$ and -7 mA pulses, the color of the bar turned black (representing $M+$) in Fig. 5(i) and gray (representing $M-$) in Fig. 5(j), respectively. The above MOKE result is consistent with the

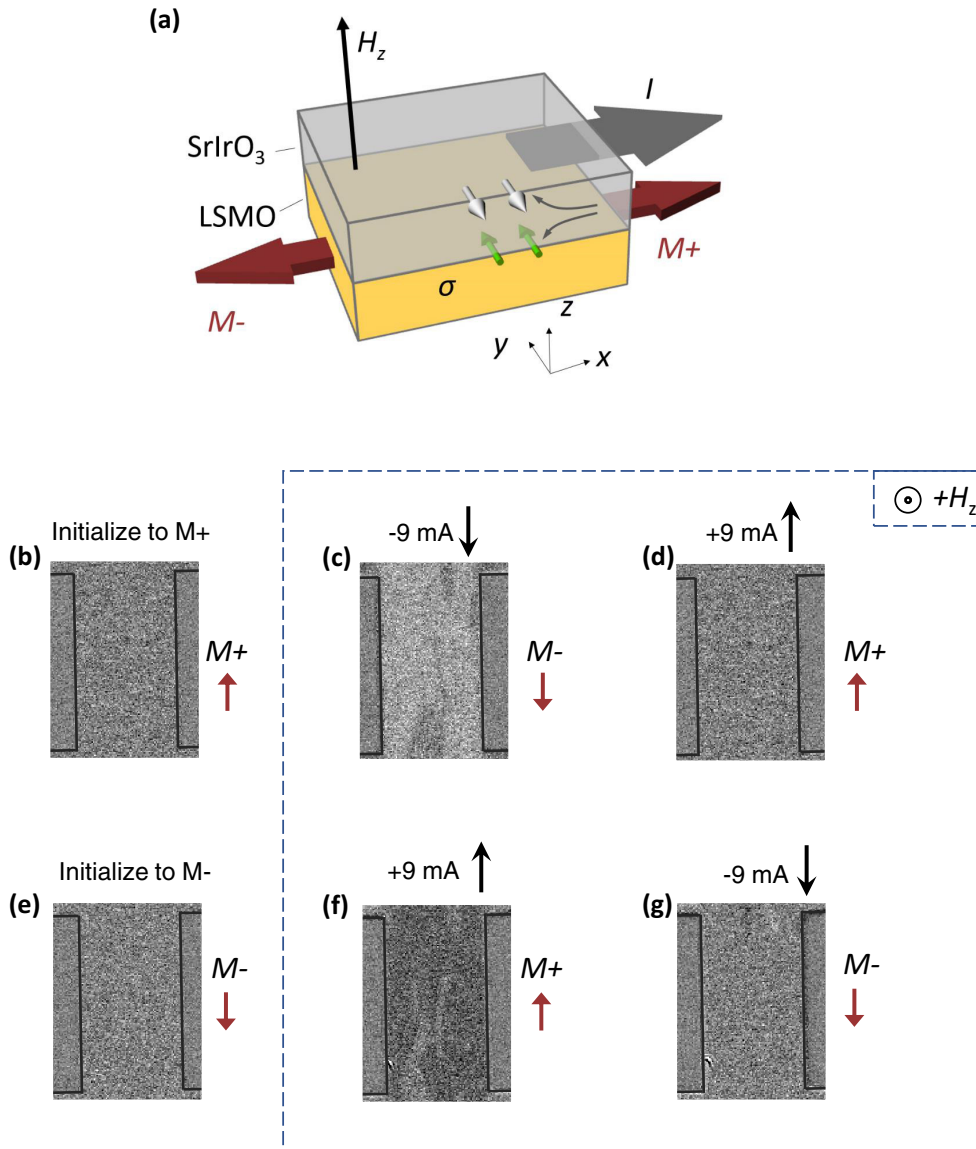


FIG. 6. Current-induced type- x spin-orbit torque (SOT) switching in SrIrO₃/LSMO bilayer. (a) Schematic illustration of the type- x SOT switching in SrIrO₃/LSMO bilayer. (b)–(g) Magnetic optical Kerr effect (MOKE) imaging of the LSMO magnetization during type- x SOT switching. The black line outlines the SrIrO₃/LSMO bar device. For processes (b)–(d), the magnetization was first initialized to $M+$ by applying a saturation field along the $+x$ direction (b). An out-of-plane field (H_z) of 200 Oe is applied to break the symmetry for (c), (d), (f), and (g). Then we applied (c) -9 mA and (d) $+9$ mA pulsed current, and the color of the bar turned white (representing $M-$) and gray (representing $M+$), respectively. For processes (e)–(g), the magnetization was first initialized to $M-$ by applying a saturation field along the $-x$ direction (e). Then we applied (f) $+9$ mA and (g) -9 mA pulsed current, and the color of the bar turned black (representing $M+$) and gray (representing $M-$), respectively. The channel width is $20 \mu\text{m}$ for the MOKE imaging.

electrical transport measurement in Fig. 5(d), demonstrating a typical type- y SOT switching [33].

Then we studied the type- x SOT switching in SrIrO₃/LSMO by fabricating a 90° bar device where the current path is aligned with the EA direction. Because the EA is in the x direction, one must apply an out-of-plane magnetic field (H_z) to break the symmetry for deterministic switching, as illustrated in Fig. 6(a). Figures 6(b)–6(g) show the MOKE imaging of the magnetization of LSMO during the type- x SOT switching. We found that, with the assistance of an out-of-plane magnetic field, the magnetization of LSMO can

be reversibly switched by applying pulsed current with an amplitude of 9 mA.

C. Current-induced effective magnetic fields

We performed the in-plane harmonic Hall voltage analysis [37] to measure the SOT efficiency in SrIrO₃/LSMO. When an ac current $I(t) = I_0 \sin(\omega t)$ is applied to the sample, the second harmonic (2ω) of the Hall voltage is related to the SOT effective fields. When the external in-plane magnetic field H_{ext} is sufficiently large to saturate M , the second harmonic (2ω)

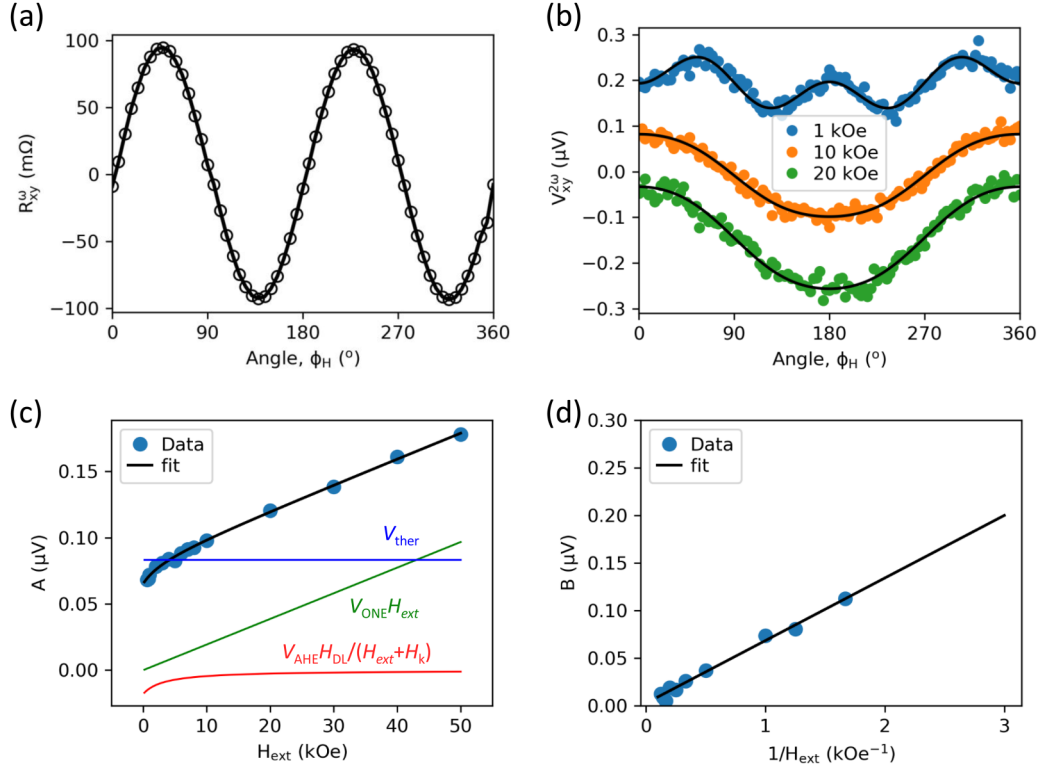


FIG. 7. Second harmonic Hall voltage analysis for SrIrO₃/LSMO bilayer. (a) The planar Hall effect. (b) In-plane angle dependence of the second harmonic Hall signal under three different H_{ext} (1, 10, and 20 kOe). The black lines are fits. (c) H_{ext} dependence of A . The black line is the fit to A using Eq. (2). The other solid lines (red, blue, and green) represent contributions from ΔB_{DL} , spin Seebeck effect (SSE) + anomalous Nernst effect (ANE), and ordinary Nernst effect (ONE), respectively. (d) $1/H_{\text{ext}}$ dependence of the fitting parameter B . The solid line is a fit using Eq. (3). An ac current of 2.6 mA is used for the measurement.

of the Hall voltage $V_{xy}^{2\omega}$ reads [37–39]

$$V_{xy}^{2\omega} = \left(\frac{V_{\text{AHE}}}{2} \frac{\Delta H_{\text{DL}}}{H_{\text{ext}} + H_{\text{K}}} + V_{\text{const}} + V_{\text{ONE}} H_{\text{ext}} \right) \cos(\phi_H) + \left(V_{\text{PHE}} \frac{\Delta H_{\text{FL}} + \Delta H_{\text{Oe}}}{H_{\text{ext}}} \right) \cos(2\phi_H) \cos(\phi_H), \quad (1)$$

where ΔH_{DL} and ΔH_{FL} are the effective fields corresponding to the dampinglike torque and the fieldlike torque, respectively. Here, V_{const} contains contributions from the spin Seebeck effect (SSE) and the anomalous Nernst effect (ANE). Also, $V_{\text{ONE}} H_{\text{ext}}$ denotes the contribution from the ordinary Nernst effect (ONE). Further, H_{K} is the out-of-plane anisotropy field. Moreover, V_{AHE} and V_{PHE} are the anomalous Hall voltage and the planar Hall voltage, respectively. The prefactors in Eq. (1) are denoted as A and B :

$$A = \frac{V_{\text{AHE}}}{2} \frac{\Delta H_{\text{DL}}}{H_{\text{ext}} + H_{\text{K}}} + V_{\text{const}} + V_{\text{ONE}} H_{\text{ext}}, \quad (2)$$

$$B = V_{\text{PHE}} \frac{\Delta H_{\text{FL}} + \Delta H_{\text{Oe}}}{H_{\text{ext}}}. \quad (3)$$

Figure 7(b) shows $V_{xy}^{2\omega}$ as a function of ϕ_H (for $H_{\text{ext}} = 1, 10, \text{ and } 20$ kOe), where the solid lines are fits to the data using Eq. (1). The fitting parameter A as a function of H_{ext} is shown in Fig. 7(c) (blue dots). The solid black line in Fig. 7(c) is the fit to A using Eq. (2). The other solid lines

(red, blue, and green) represent individual contributions from ΔH_{DL} , SSE + ANE, and ONE, respectively. Here, R_{PHE} and R_{AHE} used for the fitting are 180 mΩ [Fig. 7(a)] and 120 mΩ (Fig. 8), respectively. The out-of-plane saturation field (3.4 kOe) is used as an estimation for H_{K} (Fig. 8). We found that A shows a linear dependence with H_{ext} in the field range from 10 to 50 kOe, which indicates a large contribution from ONE, as also discovered in BiSb/FM [38,39]

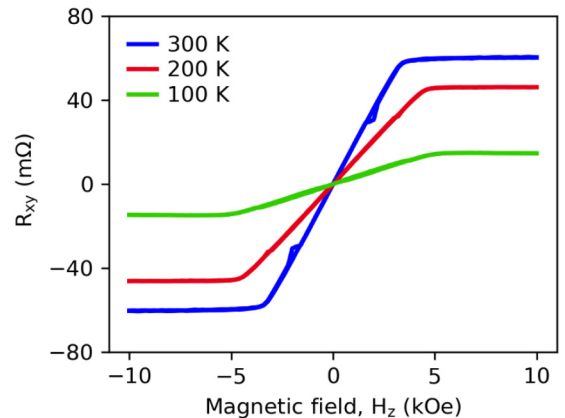


FIG. 8. Hall resistance as a function of the out-of-plane effect field measured at three different temperatures (the ordinary Hall effect has been deduced).

TABLE I. Summarized experimental parameters and fitting parameters for harmonic Hall voltage analysis in SrIrO₃/LSMO bilayer at three different temperatures.

	300 K	200 K	100 K
R_{AHE} (Ω)	0.12	0.09	0.03
R_{PHE} (Ω)	0.18	0.22	0.19
H_K (kOe)	3.3	4	5
$\Delta H_{\text{DL}}/J$ [Oe/(10 ⁶ A/cm ²)]	1.2	1.5	1.7
$(\Delta H_{\text{FL}} + \Delta H_{\text{Oe}})/J$ [Oe/(10 ⁶ A/cm ²)]	0.18	0.16	0.08
ξ_{DL}	0.15	0.19	0.21

and Pt/Cr₂Ge₂Te₆ [40] systems. The ΔH_{DL} term mainly acts at the small field range. The fitted dampinglike effective field $\Delta H_{\text{DL}}/J$ is 1.2 Oe/(10⁶ A/cm²). The second fitting parameter B as a function of $1/H_{\text{ext}}$ is shown in Fig. 7(d), where we found B is in a linear dependence on $1/H_{\text{ext}}$. The fitted $(\Delta H_{\text{FL}} + \Delta H_{\text{Oe}})/J$ is 0.18 Oe/(10⁶ A/cm²). The dampinglike SOT efficiency can be calculated using the formula: $\xi_{\text{DL}} = \frac{2eM_s t_{\text{FM}} \mu_0 \Delta H_{\text{DL}}}{\hbar J}$. The estimated ξ_{DL} is 0.15 for SrIrO₃/LSMO, comparable with that observed in metallic systems [1].

D. Temperature dependences

We measured the dampinglike SOT efficiency at different temperatures (100, 200, and 300 K). The experimental parameters (R_{AHE} , R_{PHE} , and H_K) and the fitted effective fields [$\Delta H_{\text{DL}}/J$, $(\Delta H_{\text{FL}} + \Delta H_{\text{Oe}})/J$] for different temperatures are summarized in Table I. By using the values of $\Delta H_{\text{DL}}/J$, the values of ξ_{DL} are calculated to be 0.15, 0.19, and 0.21 for 300, 200, and 100 K, respectively. Then we studied the current-induced switching at different temperatures (Fig. 9). We found two obvious trends. Firstly, the switched amplitude decreases with the decrease of the temperature, which should be due to the smaller Hall resistance at lower temperatures. Similarly, the anomalous Hall effect (R_{xy} vs H_z) also shows a decreasing trend with the decrease of the temperature (see Fig. 8). The smaller Hall signal at lower temperature is mainly due to the decrease of the normal resistivity (ρ_{xx}) of the sample. Secondly, we found that the critical switching current (I_c) increases with the decrease of the temperature, as summarized in Fig. 10(b). Although the dampinglike SOT efficiency ξ_{DL} at 100 K is ~ 1.4 times as large as that at 300 K [Fig. 10(a)], the critical switching current I_c at 100 K is much larger than that at 300 K. This should be mainly due to the large enhancement of the magnetic anisotropic energy and the saturation magnetization of the LSMO layer at 100 K compared with that at 300 K. Based on the model of a type-y SOT switching, the switch current density is proportional to the saturation magnetization M_s and the effective anisotropy field (H_K^{eff}). In our case, the estimated M_s at 100 K (~ 520 emu/cc) is ~ 2 times as large as that at 300 K (270 emu/cc). The effective anisotropy field at 100 K is ~ 1.5 times as large as that at 300 K, as estimated from Fig. 8. Therefore, the effect of the magnetic energy change on the magnetization switching is much larger than the contribution from the ξ_{DL} change, resulting in a larger I_c at lower temperatures.

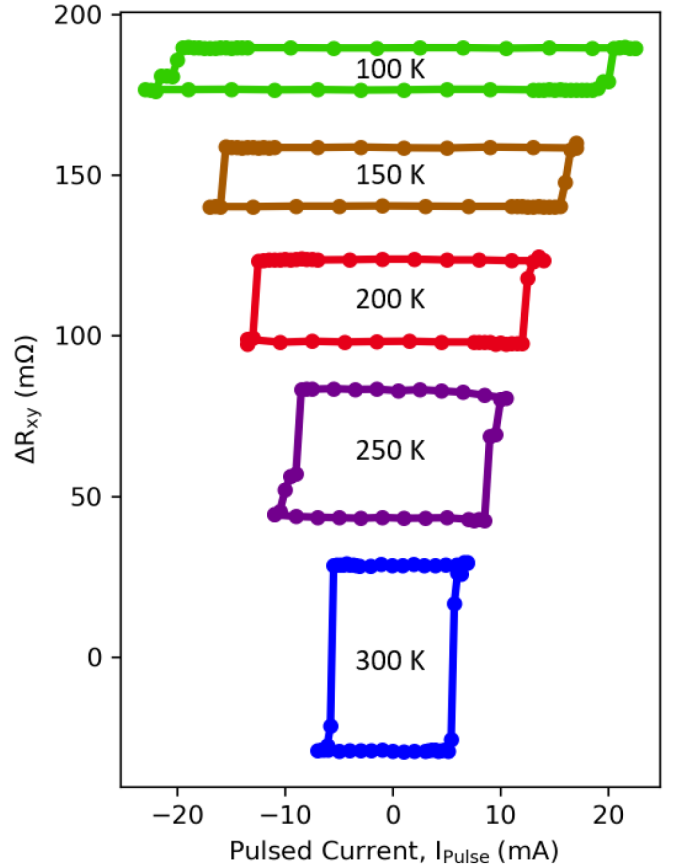


FIG. 9. Current-induced switching loops in SrIrO₃/LSMO for different temperatures.

IV. DISCUSSION AND CONCLUSIONS

We note that the Hall resistance change in Fig. 5(d) is smaller than that in Fig. 5(c), which is mainly due to the pinning effect from the Hall voltage arms. Different from the field sweeping measurement where the magnetic field can switch the magnetization of the whole pattern, the current-induced SOT switching can only switch the magnetization of the current path. Therefore, the magnetization of the two Hall arms remains unswitched, which would prevent the magnetization switching in the current path. Since the Hall signal probes the magnetization state for the whole Hall crossing area, the pinning effect results in a reduced Hall signal. To minimize the pinning effect, we fabricated a modified Hall bar device consisting of a rectangular SrIrO₃/LSMO bar and two Ti/Cu Hall voltage leads, as shown in Fig. 11(a). Figure 11(b) shows the field-driven switching loop ($\Delta R_{xy} - H_y$), and Fig. 11(c) shows the current-induced switching loop ($\Delta R_{xy} - I_{\text{pulse}}$). By comparing these two figures, a nearly complete SOT switching behavior was confirmed. We note that this modified Hall device was also used for the temperature-dependent SOT switching in Fig. 9.

As a room-temperature magnetic material, LSMO has been considered a promising candidate for oxide spintronics due to its colossal magnetoresistance [41] and half-metallic properties [42]. One fingerprint of the half-metallic property is the low magnetic damping constant ($\alpha < 8 \times 10^{-4}$) [19].

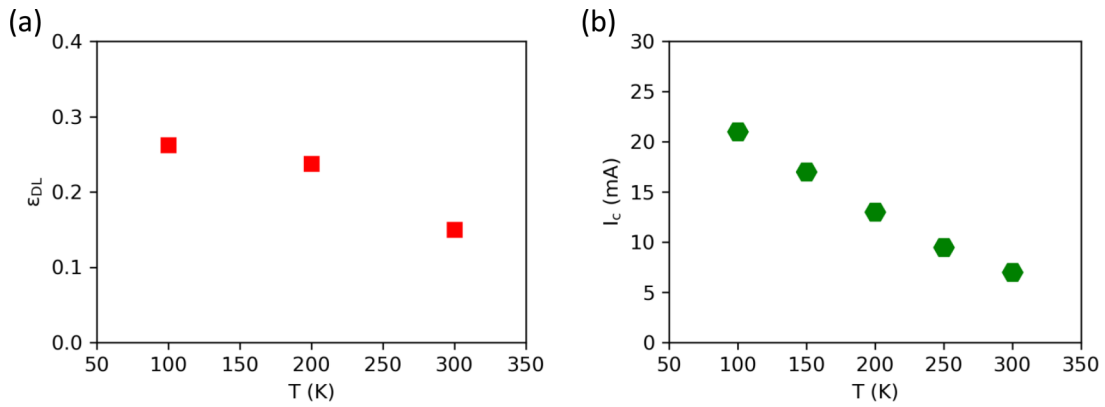


FIG. 10. Temperature dependences of (a) the dampinglike spin-orbit torque (SOT) efficiency and (b) the critical switching current for SrIrO₃/LSMO.

According to the spin Hall effect–SOT switching scenario in bilayers with in-plane magnetic anisotropy [33], spin sources with high θ_{SH} and magnetic materials with low α and low M_s are pursued to lower the switching current density J_{sw} , for which the all-oxide SrIrO₃/LSMO may give an ideal choice. Although the damping constant of LSMO will be enhanced when it is adjacent to a spin source layer, $\alpha \sim 0.005$ for SrIrO₃/LSMO is still smaller than that for typical metallic

SOT bilayers such as Pt/Co ($\alpha \sim 0.02\text{--}0.1$). The low α and the low M_s properties result in a low energy barrier such that we can fully switch an LSMO with a thickness of 15 nm, much thicker than that of the Co layer used for SOT switching [1]. Recently, it was found that LSMO can be used for magnon devices with long spin-wave propagation in artificial antiferromagnetic strips [43,44]. By combining the efficient tool of current-induced SOT and the superior magnetic properties of

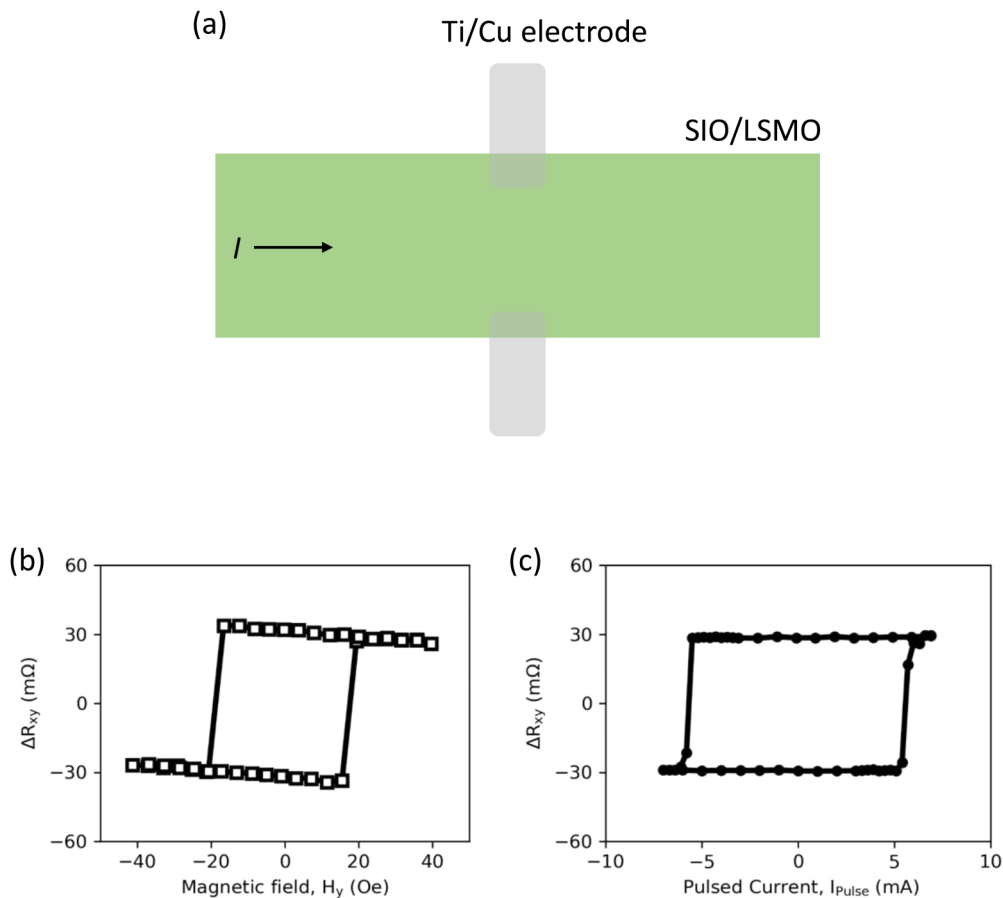


FIG. 11. Current-induced switching in the modified SrIrO₃/LSMO Hall bar. (a) Modified Hall bar devices with Ti/Cu Hall voltage leads to minimize the pinning effect. (b) Magnetic-field-induced switching of the magnetization. (c) Current-induced switching of the magnetization. $H_x = 30$ Oe is used for the measurement.

LSMO, we believe it is very promising to develop types of LSMO-based spintronics devices.

In summary, we designed an all-oxide SrIrO₃/LMSO bilayer for SOT switching. By controlling the in-plane magnetocrystalline anisotropy of LSMO, we realized two types of SOT switching in SrIrO₃/LSMO at room temperature. Given the big family of oxide materials, there is a large space to improve the SOT switching performance in all-oxide heterostructures, for example, by engineering the SOT strength through epitaxial strain-mediated octahedral rotation, minimizing the current-shunting effect by choosing FM insulators, and designing a magnon-torque device using oxide trilayer structures. In this regard, we anticipate the realization of current-induced magnetization switching in SrIrO₃/LSMO

may stimulate following SOT studies in a wide variety of all-oxide structures and generate types of oxide spintronics devices.

ACKNOWLEDGMENTS

This paper is supported by the Singapore Ministry of Education MOE2018-T2-2-043, MOE Tier 1 22-4888-A0001, A*STAR AMEIRG18-0022, MOE Tier 2 MOE-T2EP50121-0011, A*STAR A1983C0036, and Singapore National Research Foundation under CRP Award (Grant No. NRF-CRP23-2019-0070). G.Z. and X.X. acknowledge the National Natural Science Foundation of China (No. 51901118 and No. 51871137).

-
- [1] L. Liu, C.-F. Pai, Y. Li, H. W. Tseng, D. C. Ralph, and R. A. Buhrman, Spin-torque switching with the giant spin Hall effect of tantalum, *Science* **336**, 555 (2012).
- [2] I. M. Miron, K. Garello, G. Gaudin, P. J. Zermatten, M. V. Costache, S. Auffret, S. Bandiera, B. Rodmacq, A. Schuhl, and P. Gambardella, Perpendicular switching of a single ferromagnetic layer induced by in-plane current injection, *Nature (London)* **476**, 189 (2011).
- [3] A. R. Mellnik, J. S. Lee, A. Richardella, J. L. Grab, P. J. Mintun, M. H. Fischer, A. Vaezi, A. Manchon, E. A. Kim, N. Samarth *et al.*, Spin-transfer torque generated by a topological insulator, *Nature (London)* **511**, 449 (2014).
- [4] Z. Qiu, T. An, K. Uchida, D. Hou, Y. Shiomi, Y. Fujikawa, and E. Saitoh, Experimental investigation of spin Hall effect in indium tin oxide thin film, *Appl. Phys. Lett.* **103**, 182404 (2013).
- [5] K. Fujiwara, Y. Fukuma, J. Matsuno, H. Idzuchi, Y. Niimi, Y. Otani, and H. Takagi, 5d iridium oxide as a material for spin-current detection, *Nat. Commun.* **4**, 2893 (2013).
- [6] E. Lesne, Y. Fu, S. Oyarzun, J. C. Rojas-Sánchez, D. C. Vaz, H. Naganuma, G. Sicoli, J. P. Attané, M. Jamet, E. Jacquet *et al.*, Highly efficient and tunable spin-to-charge conversion through Rashba coupling at oxide interfaces, *Nat. Mater.* **15**, 1261 (2016).
- [7] T. Nan, T. J. Anderson, J. Gibbons, K. Hwang, N. Campbell, H. Zhou, Y. Q. Dong, G. Y. Kim, D. F. Shao, T. R. Paudel *et al.*, Anisotropic spin-orbit torque generation in epitaxial SrIrO₃ by symmetry design, *Proc. Natl. Acad. Sci. USA* **116**, 16186 (2019).
- [8] A. S. Everhardt, M. DC, X. Huang, S. Sayed, T. A. Gosavi, Y. Tang, C.-C. Lin, S. Manipatruni, I. A. Young, S. Datta *et al.*, Tunable charge to spin conversion in strontium iridate thin films, *Phys. Rev. Materials* **3**, 051201(R) (2019).
- [9] Y. Ou, Z. Wang, C. S. Chang, H. P. Nair, H. Paik, N. Reynolds, D. C. Ralph, D. A. Muller, D. G. Schlom, and R. A. Buhrman, Exceptionally high, strongly temperature dependent, spin Hall conductivity of SrRuO₃, *Nano. Lett.* **19**, 3663 (2019).
- [10] J. Zhou, X. Shu, W. Lin, D. F. Shao, S. Chen, L. Liu, P. Yang, E. Y. Tsymlal, and J. Chen, Modulation of spin-orbit torque from SrRuO₃ by epitaxial-strain-induced octahedral rotation, *Adv. Mater.* **33**, 2007114 (2021).
- [11] J. Wei, H. Zhong, J. Liu, X. Wang, F. Meng, H. Xu, Y. Liu, X. Luo, Q. Zhang, Y. Guang *et al.*, Enhancement of spin-orbit torque by strain engineering in SrRuO₃ films, *Adv. Func. Mater.* **31**, 2100380 (2021).
- [12] C. Y. Guo, C. H. Wan, M. K. Zhao, H. Wu, C. Fang, Z. R. Yan, J. F. Feng, H. F. Liu, and X. F. Han, Spin-orbit torque switching in perpendicular Y₃Fe₅O₁₂/Pt bilayer, *Appl. Phys. Lett.* **114**, 192409 (2019).
- [13] C. O. Avci, A. Quindeau, C.-F. Pai, M. Mann, L. Caretta, A. S. Tang, M. C. Onbasli, C. A. Ross, and G. S. D. Beach, Current-induced switching in a magnetic insulator, *Nat. Mater.* **16**, 309 (2017).
- [14] X. Z. Chen, R. Zarzuela, J. Zhang, C. Song, X. F. Zhou, G. Y. Shi, F. Li, H. A. Zhou, W. J. Jiang, F. Pan *et al.*, Antidamping-Torque-Induced Switching in Biaxial Antiferromagnetic Insulators, *Phys. Rev. Lett.* **120**, 207204 (2018).
- [15] Y. Cheng, S. Yu, M. Zhu, J. Hwang, and F. Yang, Electrical Switching of Tristate Antiferromagnetic Néel Order in Fe₂O₃ Epitaxial Films, *Phys. Rev. Lett.* **124**, 027202 (2020).
- [16] H. K. Lee, I. Barsukov, A. G. Swartz, B. Kim, L. Yang, H. Y. Hwang, and I. N. Krivorotov, Magnetic anisotropy, damping, and interfacial spin transport in Pt/LSMO bilayers, *AIP Adv.* **6**, 055212 (2016).
- [17] S. Seki, T. Ideue, M. Kubota, Y. Kozuka, R. Takagi, M. Nakamura, Y. Kaneko, M. Kawasaki, and Y. Tokura, Thermal Generation of Spin Current in an Antiferromagnet, *Phys. Rev. Lett.* **115**, 266601 (2015).
- [18] H. Chang, P. Li, W. Zhang, T. Liu, A. Hoffmann, L. Deng, and M. Wu, Nanometer-thick yttrium iron garnet films with extremely low damping, *IEEE Mag. Lett.* **5**, 1 (2014).
- [19] Q. Qin, S. He, W. Song, P. Yang, Q. Wu, Y. P. Feng, and J. Chen, Ultra-low magnetic damping of perovskite La_{0.7}Sr_{0.3}MnO₃ thin films, *Appl. Phys. Lett.* **110**, 112401 (2017).
- [20] Y. Kajiwara, K. Harii, S. Takahashi, J. Ohe, K. Uchida, M. Mizuguchi, H. Umezawa, H. Kawai, K. Ando, K. Takanashi *et al.*, Transmission of electrical signals by spin-wave interconversion in a magnetic insulator, *Nature (London)* **464**, 262 (2010).
- [21] H. Wang, C. Du, P. C. Hammel, and F. Yang, Antiferromagnonic Spin Transport from Y₃Fe₅O₁₂ into NiO, *Phys. Rev. Lett.* **113**, 097202 (2014).

- [22] R. Lebrun, A. Ross, S. A. Bender, A. Qaiumzadeh, L. Baldrati, J. Cramer, A. Brataas, R. A. Duine, and M. Kläui, Tunable long-distance spin transport in a crystalline antiferromagnetic iron oxide, *Nature (London)* **561**, 222 (2018).
- [23] M. Wahler, N. Homonnay, T. Richter, A. Müller, C. Eiseenschmidt, B. Fuhrmann, and G. Schmidt, Inverse spin Hall effect in a complex ferromagnetic oxide heterostructure, *Sci. Rep.* **6**, 28727 (2016).
- [24] L. Liu, Q. Qin, W. Lin, C. Li, Q. Xie, S. He, X. Shu, C. Zhou, Z. Lim, J. Yu *et al.*, Current-induced magnetization switching in all-oxide heterostructures, *Nat. Nanotechnol.* **14**, 939 (2019).
- [25] S. Ohya, D. Araki, L. D. Anh, S. Kaneta, M. Seki, H. Tabata, and M. Tanaka, Efficient intrinsic spin-to-charge current conversion in an all-epitaxial single-crystal perovskite-oxide heterostructure of $\text{La}_{0.67}\text{Sr}_{0.33}\text{MnO}_3/\text{LaAlO}_3/\text{SrTiO}_3$, *Phys. Rev. Research* **2**, 012014(R) (2020).
- [26] S. Crossley, A. G. Swartz, K. Nishio, Y. Hikita, and H. Y. Hwang, All-oxide ferromagnetic resonance and spin pumping with SrIrO_3 , *Phys. Rev. B* **100**, 115163 (2019).
- [27] M. Yamanouchi, T. Oyamada, and H. Ohta, Current-induced effective magnetic field in $\text{La}_{0.67}\text{Sr}_{0.33}\text{MnO}_3/\text{LaAlO}_3/\text{SrTiO}_3$ structures, *AIP Adv.* **10**, 015129 (2020).
- [28] T. Richter, M. Paleschke, M. Wahler, F. Heyroth, H. Deniz, D. Hesse, and G. Schmidt, Spin pumping and inverse spin Hall effect in ultrathin SrRuO_3 films around the percolation limit, *Phys. Rev. B* **96**, 184407 (2017).
- [29] X. Huang, S. Sayed, J. Mittelstaedt, S. Susarla, S. Karimeddiny, L. Caretta, H. Zhang, V. A. Stoica, T. Gosavi, F. Mahfouzi *et al.*, Novel spin-orbit torque generation at room temperature in an all-oxide epitaxial $\text{La}_{0.7}\text{Sr}_{0.3}\text{MnO}_3/\text{SrIrO}_3$ system, *Adv. Mater.* **33**, 2008269 (2021).
- [30] F. Trier, P. Noël, J. V. Kim, J.-P. Attané, L. Vila, and M. Bibes, Oxide spin-orbitronics: spin-charge interconversion and topological spin textures, *Nat. Rev. Mater.* **7**, 258 (2022).
- [31] H. Boschker, M. Mathews, E. P. Houwman, H. Nishikawa, A. Vailionis, G. Koster, G. Rijnders, and D. H. A. Blank, Strong uniaxial in-plane magnetic anisotropy of (001)- and (011)-oriented $\text{La}_{0.67}\text{Sr}_{0.33}\text{MnO}_3$ thin films on NdGaO_3 substrates, *Phys. Rev. B* **79**, 214425 (2009).
- [32] A. Vailionis, H. Boschker, W. Siemons, E. P. Houwman, D. H. A. Blank, G. Rijnders, and G. Koster, Misfit strain accommodation in epitaxial ABO_3 perovskites: lattice rotations and lattice modulations, *Phys. Rev. B* **83**, 064101 (2011).
- [33] S. Fukami, T. Anekawa, C. Zhang, and H. Ohno, A spin-orbit torque switching scheme with collinear magnetic easy axis and current configuration, *Nat. Nanotechnol.* **11**, 621 (2016).
- [34] Y. Wang, D. Zhu, Y. Wu, Y. Yang, J. Yu, R. Ramaswamy, R. Mishra, S. Shi, M. Elyasi, K.-L. Teo *et al.*, Room temperature magnetization switching in topological insulator-ferromagnet heterostructures by spin-orbit torques, *Nat. Commun.* **8**, 1364 (2017).
- [35] G. Mihajlović, O. Mosendz, L. Wan, N. Smith, Y. Choi, Y. Wang, and J. A. Katine, Pt thickness dependence of spin Hall effect switching of in-plane magnetized CoFeB free layers studied by differential planar Hall effect, *Appl. Phys. Lett.* **109**, 192404 (2016).
- [36] Y. Takahashi, Y. Takeuchi, C. Zhang, B. Jinnai, S. Fukami, and H. Ohno, Spin-orbit torque-induced switching of in-plane magnetized elliptic nanodot arrays with various easy-axis directions measured by differential planar Hall resistance, *Appl. Phys. Lett.* **114**, 012410 (2019).
- [37] C. O. Avci, K. Garello, M. Gabureac, A. Ghosh, A. Fuhrer, S. F. Alvarado, and P. Gambardella, Interplay of spin-orbit torque and thermoelectric effects in ferromagnet/normal-metal bilayers, *Phys. Rev. B* **90**, 224427 (2014).
- [38] N. Roschewsky, E. S. Walker, P. Gowtham, S. Muschinske, F. Hellman, S. R. Bank, and S. Salahuddin, Spin-orbit torque and Nernst effect in Bi-Sb/Co heterostructures, *Phys. Rev. B* **99**, 195103 (2019).
- [39] Z. Chi, Y.-C. Lau, X. Xu, T. Ohkubo, K. Hono, and M. Hayashi, The spin Hall effect of Bi-Sb alloys driven by thermally excited Dirac-like electrons, *Sci. Adv.* **6**, eaay2324 (2020).
- [40] V. Gupta, T. M. Cham, G. M. Stiehl, A. Bose, J. A. Mittelstaedt, K. Kang, S. Jiang, K. F. Mak, J. Shan, R. A. Buhrman *et al.*, Manipulation of the van der Waals magnet $\text{Cr}_2\text{Ge}_2\text{Te}_6$ by spin-orbit torques, *Nano. Lett.* **20**, 7482 (2020).
- [41] A. P. Ramirez, Colossal magnetoresistance, *J. Phys. Condens. Matter* **9**, 8171 (1997).
- [42] J. H. Park, E. Vescovo, H. J. Kim, C. Kwon, R. Ramesh, and T. Venkatesan, Direct evidence for a half-metallic ferromagnet, *Nature (London)* **392**, 794 (1998).
- [43] J. Wang, S. Wu, J. Ma, L. Xie, C. Wang, I. A. Malik, Y. Zhang, K. Xia, C.-W. Nan, and J. Zhang, Nanoscale control of stripe-ordered magnetic domain walls by vertical spin transfer torque in $\text{La}_{0.67}\text{Sr}_{0.33}\text{MnO}_3$ film, *Appl. Phys. Lett.* **112**, 072408 (2018).
- [44] C. Liu, S. Wu, J. Zhang, J. Chen, J. Ding, J. Ma, Y. Zhang, Y. Sun, S. Tu, H. Wang *et al.*, Current-controlled propagation of spin waves in antiparallel, coupled domains, *Nat. Nanotechnol.* **14**, 691 (2019).